RESEARCH ARTICLE
SPACE PHYSICS

Earth and Planetary Physics
10: 427–437, 2026
doi: 10.26464/epp2026036

OH airglow imaging observations of a mesoscale gravity wave generated by jet streams near the Tibetan Plateau region

QinZeng Li[1*], YiLin Liu[1,2], JiYao Xu[1], Wei Yuan[1], YaYun Zhu[1], and Xiao Liu[3]

[1]State Key Laboratory of Solar Activity and Space Weather, National Space Science Center, Chinese Academy of Sciences, Beijing 100190, China;

[2]College of Earth and Planetary Sciences, University of Chinese Academy of Sciences, Beijing, 100049, China;

[3]School of Mathematics and Statistics, Henan Normal University, Xinxiang Henan 453000, China

Key Points:

- We observed a mesoscale gravity wave (MGW) in the mesosphere and lower thermosphere region by using an OH airglow imager at Xinglong.
- Backward ray-tracing analysis revealed that the MGW was generated by the jet system in the troposphere near the Tibetan Plateau region.
- The propagation of the MGW accompanied by strong instability may be caused by wind shear.

Citation: Li, Q. Z., Liu, Y. L., Xu, J. Y., Yuan, W., Zhu, Y. Y., and Liu, X. (2026). OH airglow imaging observations of a mesoscale gravity wave generated by jet streams near the Tibetan Plateau region. *Earth Planet. Phys.*, *10*(3), 427–437. http://doi.org/10.26464/epp2026036

Abstract: In this study, we investigate the source and dynamics of a mesoscale gravity wave (MGW) observed over northern China. On January 12, 2010, an OH airglow imager at the Xinglong station (40.2°N, 117.4°E) detected an MGW propagating from southwest to northeast, consistent with the background wind direction. The wave exhibited a horizontal wavelength of 125 ± 7.6 km, an observed period of 25 ± 3.2 min, and a phase speed of 83 ± 12.4 m/s. The momentum flux and the energy flux of the MGW were approximately 24.93 m^2/s^2 and 1.08×10^{-5} W/m^2, respectively, from the airglow imaging observation. During propagation, wave breaking generated secondary ripples with wavelengths of 5–12 km. These ripples were likely caused by wind shear, as measured by the Doppler meteor radar at Shisanling (40.3°N, 116.2°E). According to OH emission profiles from the Sounding of the Atmosphere using Broadband Emission Radiometry (SABER) instrument on board the Thermosphere Ionosphere Mesosphere Energetics and Dynamics (TIMED) satellite, the height of the OH airglow layer was ~81 km during the MGW propagation event. A separate northwestward-propagating small-scale gravity wave with a wavelength of ~35 km was also observed. The backward ray-tracing analysis conducted with European Centre for Medium-Range Weather Forecasts (ECMWF) ERA5 reanalysis data indicated that the jet system near the Tibetan Plateau served as the source for the MGW.

Keywords: airglow; mesoscale gravity wave; ripple; jet system

---

1. Introduction

Gravity waves (GWs) are mainly generated by flow over orography (Wright et al., 2017; Geldenhuys et al., 2021), convection (Fovell et al., 1992; Alexander and Holton, 2004; Nyassor et al., 2022; Franco-Diaz et al., 2024; Li QZ et al., 2025a), a front–jet stream (Fritts and Nastrom, 1992; Jia MJ et al., 2016; Li QZ et al., 2018; Xue XH et al., 2020; Wrasse et al., 2024), and wind shear in the troposphere (Fritts, 1982; Pramitha et al., 2015; Chen YX et al., 2026). Solar eclipses can also generate GWs (Chen G et al., 2011; Nayak and Yiğit, 2018; Gu SY et al., 2023). GWs play an important role in driving global-scale circulation in the mesosphere and lower thermosphere (MLT) region via momentum and energy deposition (Fritts and Alexander, 2003; Gao HY et al., 2018; Ern et al., 2022; Gavrilov et al., 2022; Plane et al., 2023; Nyassor et al., 2025).

The technique of all-sky airglow imaging enables the detection of GWs by observing the perturbations in nighttime airglow emissions (Ghodpage et al., 2016; Wüst et al., 2019, 2023). The parameters of the GWs (horizontal wavelengths, phase velocities, and observed periods) can be retrieved from two-dimensional airglow images (Li QZ et al., 2011). The vertical wavelengths can be obtained by using the GW dispersion relation. Through the all-sky airglow imaging technique, we can gain a better understanding of the dynamical processes in the MLT region. Although a number of airglow imaging observations have been reported, a comprehensive understanding of the characteristics of high-frequency GWs remains unclear.

Small-scale GWs, which range from several kilometers to tens of kilometers, are frequently observed and studied using a single airglow imaging instrument (Smith et al., 2000; Ejiri et al., 2003; Nielsen et al., 2009; Li QZ et al., 2011, 2016, 2018, 2025b), whereas

---

Correspondence to: Q. Z. Li, qzli@swl.ac.cn
Received 27 NOV 2025; Accepted 27 JAN 2026.

a mesoscale gravity wave (MGW), which spans hundreds of kilometers, is seldom detected by a single such instrument. Atmospheric GWs with horizontal wavelengths exceeding approximately 200 km are challenging to characterize when using a single-station airglow imager owing to field-of-view constraints and the reduced sensitivity to longer spatial gradients. A networked observation is typically required for their unambiguous detection and analysis (Li QZ et al., 2022, 2024).

In this work, we used a backward ray-tracing analysis to locate the possible source of an MGW. Analysis of reanalysis data from the European Centre for Medium Range Weather Forecasts (ECMWF) ERA5 indicates that the jet system was the source of the MGW observed by an OH airglow imager at the Xinglong station (40.2°N, 117.4°E) on the night of January 12, 2010.

2. Instruments and Methodology

The Meridian Project all-sky airglow imager located at the Xinglong station (40.2°N, 117.4°E; red star in Figure 1) utilizes a Mamiya 24 mm/f4.0 fisheye lens providing a 180° field of view. The detector is a back-illuminated CCD (charge-coupled device) camera with 1024 × 1024 pixels and physical dimensions of 13.3 × 13.3 mm. The system incorporates a temperature-stabilized eight-position filter wheel. For this study, only observations using the OH band emission filter were utilized. This filter has a bandpass of 715–930 nm and includes a notch at 865.5 nm to suppress the O_2 (0, −1) atmospheric band emission. The OH images were acquired with an exposure time of 1 min. The airglow image processing methodology involved the following sequential steps (Li QZ et al., 2011): First, we applied a median filter with a 15 × 15 pixel window to raw images to remove stars, and we subtracted dark current noise using previously acquired dark frames. Atmospheric corrections for the van Rhijn effect (zenith-angle-dependent intensity variations) and extinction (light absorption/scattering) were applied via the methodology of Kubota et al. (2001). This method determines a key extinction coefficient by fitting observed and theoretical intensity profiles; the coefficient is then used for flat-field correction. Approximately 30% of atmospheric background emissions were subtracted based on established ratios from Suzuki et al. (2007). Finally, spatial calibration mapped original pixel coordinates to standardized coordinates through a star-referenced linear transformation with least-squares fitting (Hapgood and Taylor, 1982; Garcia et al., 1997), followed by projection to geographic coordinates assuming an 81 km emission height for the OH airglow layer. This height value is justified in Figure 4a based on Thermosphere Ionosphere Mesosphere Energetics and Dynamics (TIMED)/Sounding of the Atmosphere using Broadband Emission Radiometry (SABER) observations of OH peak emission altitudes. Background wind data in the MLT region were obtained using a meteor radar located at Shisanling (40.3°N, 116.2°E; red triangle in Figure 1). This system operates at a frequency of 38.9 MHz with a transmission power of 7.5 kW and a pulse repetition frequency of 430 Hz (Holdsworth et al., 2004). The radar provides wind speed measurements at altitudes between 70 and 110 km, typically derived from 1 h integrations with a vertical resolution of 2 km.

The background temperature and emission data in the MLT region were obtained from the SABER instrument onboard NASA's TIMED satellite (Mertens et al., 2001), launched on December 7, 2001. The SABER instrument is a 10-channel limb-scanning infrared radiometer (1.27–17 μm spectral range) that retrieves kinetic temperatures with ±2–5 K accuracy. Temperature measurements derive from CO_2 emissions at 15 μm below 90 km and 4.3 μm above 90 km. The red asterisks in Figure 1 denote the TIMED/SABER descending footprints on the night of January 12–13, 2010.

The atmospheric temperature and wind data below the MLT region utilized in this study were sourced from the ERA5 reanalysis dataset (Hersbach et al., 2020). As ECMWF's fifth-generation reanalysis, ERA5 assimilates observations using a 4D-Var (four-dimensional variational) system integrated into its Integrated Forecasting System. The data used have a native horizontal grid resolution of 0.25° × 0.25° and an hourly output frequency, and are provided on 137 hybrid sigma-pressure vertical levels extending from the surface up to 0.01 hPa (approximately 80 km altitude).

3. Results and Discussion

3.1 Characteristics of the Waves

An MGW was observed by an OH airglow imager at the Xinglong station on the night of January 12, 2010. Figure 2 shows a series of time-difference images projected onto a 500 × 500 km grid. The dashed lines mark the wave phases propagating northeastward. The observed horizontal wavelength, period, and phase speed are 125 ± 7.6 km, 25 ± 3.2 min, and 83 ± 12.4 m/s, respectively. We identified numerous small-scale structures—ripples (marked by yellow circles) with wavelengths of 5–12 km—indicating wave breaking of the MGW. The fronts of these ripples are inclined at an

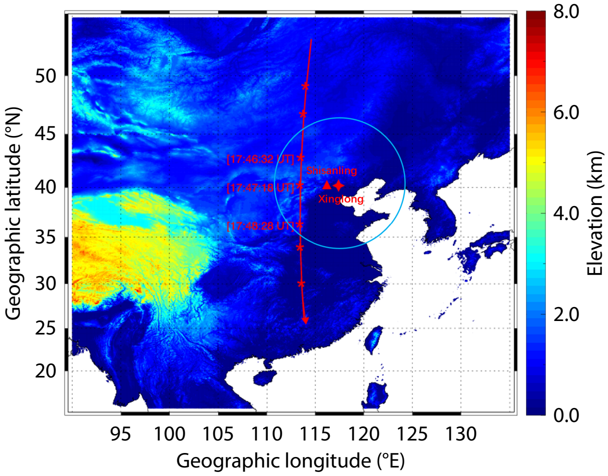

Figure 1. The locations of the airglow imager station at Xinglong (red star) and meteor radar station at Shisanling (red triangle). The circle on the map gives the effective observation ranges of the OH airglow imager with a 172° field of view. The red asterisks denote the TIMED/SABER descending footprints on January 12, 2010. The background presents the map of topography elevation from GTOPO30.

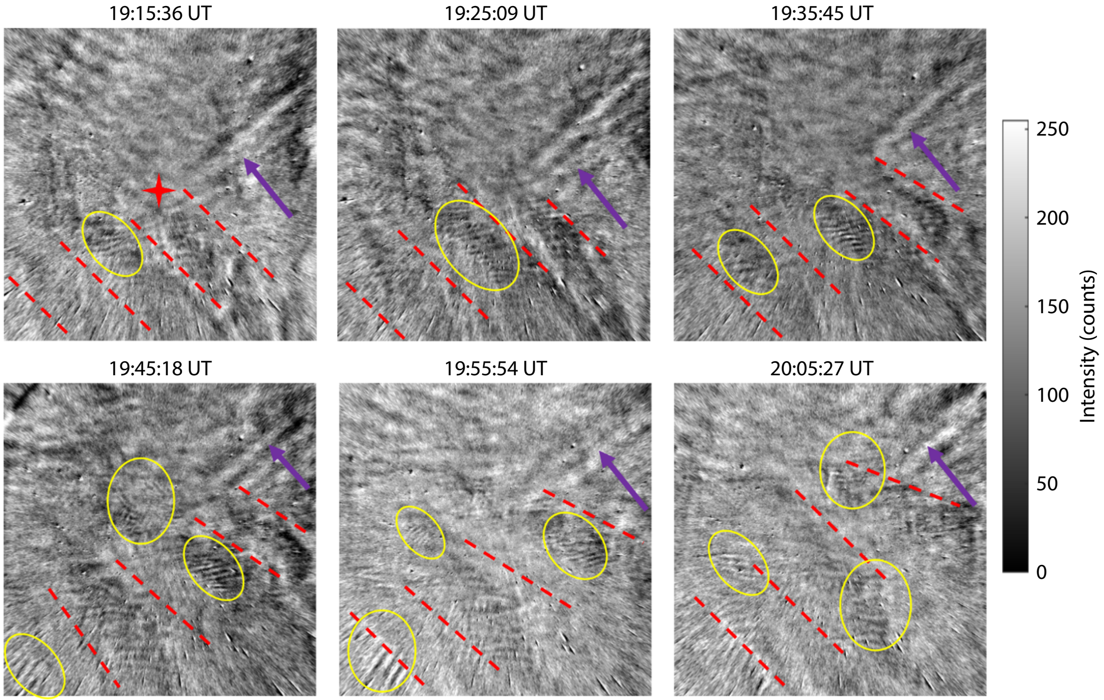

Figure 2. The 500 × 500 km time difference OH images from 19:15:36 UT to 20:05:27 UT on January 12, 2010. The dashed red lines mark the phases of the MGW. The purple arrows indicate GWs propagating northwestward. The areas marked by yellow circles are instability structures.

angle to those of the MGW. In Figure 2, the ripple fronts marked in the lower left corner at 19:45:18 universal time (UT) and 19:55:54 UT are almost perpendicular to the MGW fronts. In addition, we observed a small-scale GW propagating toward the northwest direction (indicated by the purple arrow), with a horizontal wavelength of approximately 35 km, an observation period of approximately 16 min, and a phase speed of approximately 36 m/s.

To highlight the mesoscale fluctuations more clearly, we applied bandpass filtering ranging from 100 to 150 km as shown in Figure 3. We found that the outlines of the MGW became much more distinct.

Figures 4a and 4b show the OH 1.6 μm emission and temperature derived from TIMED/SABER at 17:46:32 UT (black), 17:47:18 UT (blue), 17:48:28 UT (green) on the night of January 12, 2010, respectively. The red profile gives the average result. The OH emission height peaks at approximately 81 km.

The square of the Brunt–Väisälä frequency N^2 derived from the temperature is given by

$$N^2 = \frac{g}{T}\left(\frac{\mathrm{d}T}{\mathrm{d}z} + \frac{g}{c_p}\right), \tag{1}$$

where g is the gravitational acceleration, $c_p = 1005\ \mathrm{J\ kg^{-1}\ K^{-1}}$ is the specific heat at constant pressure, T is the temperature from the TIMED/SABER observations, and $\mathrm{d}T/\mathrm{d}z$ is the vertical temperature gradient. Figure 4c shows the square of the Brunt–Väisälä frequency N^2 derived from the average temperature profile in Figure 4b. The vertical wavenumbers $\left(m = \frac{2\pi}{\lambda_z}\right)$ of the GWs are estimated by using the GW dispersion relation (Hines, 1960):

$$m^2 = \frac{N^2}{(c-u)^2} - k^2 - \frac{1}{4H^2}, \tag{2}$$

where $k = \frac{2\pi}{\lambda_x}$ is the horizontal wavenumber, c is the observed phase speed of the wave, u is the wind speed in the wave direction derived from meteor radar, and H is the scale height calculated from temperatures observed by TIMED/SABER. Using Equation (2), we investigated the propagation nature of the MGW. Figure 4d shows the wind speed in the wave direction derived from meteor radar, indicating that the background wind was essentially aligned with the propagation direction of the wave. Figure 4e shows the square of the vertical wavenumber m^2.

We can use airglow imaging observations to estimate the GW momentum flux (F_M) and energy flux (F_E). The F_M and F_E equations (Swenson and Liu AZ, 1998) are expressed as

$$F_M = \frac{1}{2}\frac{g^2}{N^2}\frac{\lambda_z}{\lambda_x}\left(\frac{I'}{\bar{I}}\right)^2\frac{1}{CF^2}, \tag{3}$$

$$F_E = \frac{1}{2}\frac{\rho}{\tau_b}\frac{g^2}{N^2}\frac{\lambda_z^2}{\lambda_x}\left(\frac{I'}{\bar{I}}\right)^2\frac{1}{CF^2}, \tag{4}$$

where F_M is in $\mathrm{m^2{\cdot}s^{-2}}$, F_E is in $\mathrm{W{\cdot}m^{-2}}$; $CF = 3.5 - (3.5 - 0.1)\times \exp[-0.0055(\lambda_z - 6)^2]$ is the cancellation factor; I' is the perturbed airglow intensity; $\bar{I}$ is the averaged airglow intensity; ρ is the mass density of the atmosphere; τ_b is the Brunt–Väisälä period; and λ_x and λ_z are the horizontal wavelength and vertical wavelength, respectively. The relative intensity perturbation of the MGW was found to be ~2.0%. The mean F_M was determined to be 24.93 $\mathrm{m^2/s^2}$, which is comparatively larger than the momentum fluxes reported by studies of the MGWs generated by the polar jet (Suzuki et al., 2013) and jet–front (Jia MJ et al., 2016). The F_E of the

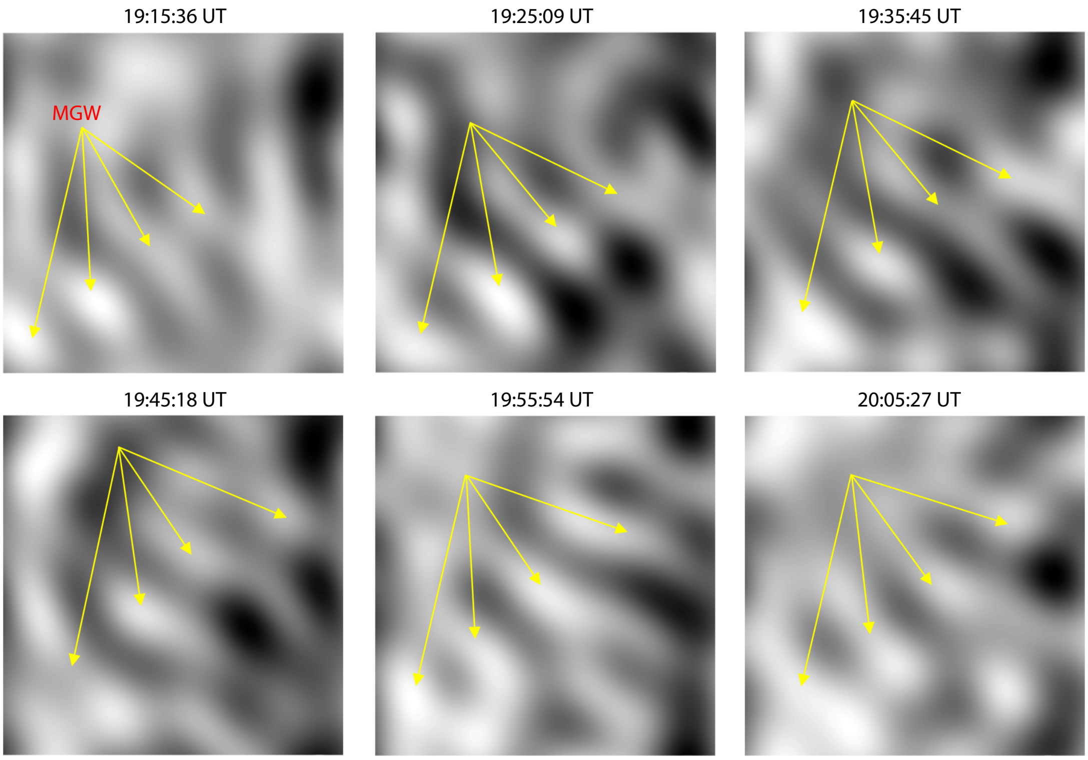

Figure 3. Similar to Figure 2, but with bandpass filtering applied between 100 and 150 km.

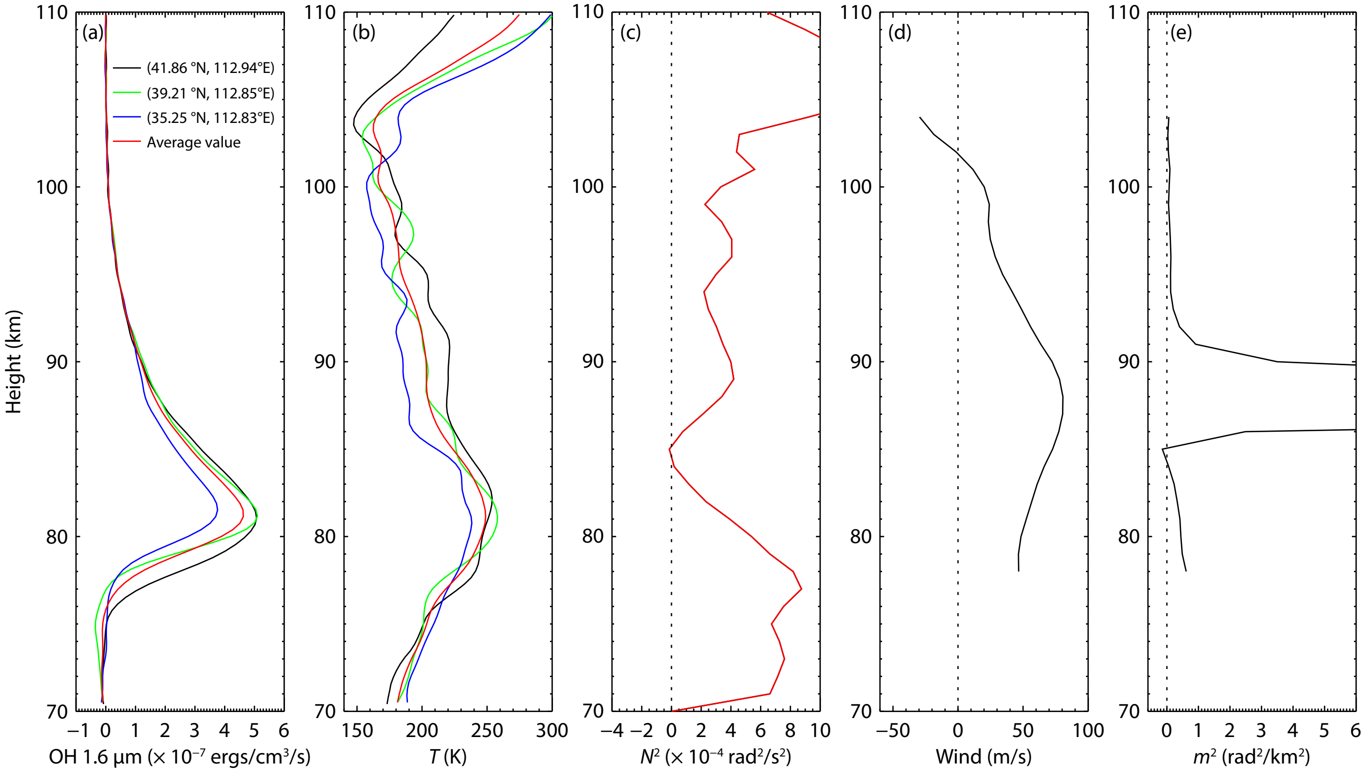

Figure 4. (a) OH 1.6 μm emission and (b) temperature derived from TIMED/SABER at 17:46:32 UT (black), 17:47:18 UT (blue), and 17:48:28 UT (green) on January 12, 2010. The red profile gives the average result. (c) The square of the Brunt–Väisälä frequency N^2 derived from the average temperature profile in (b). (d) The averaged meteor radar wind profile in the wave propagation direction from 18:00 to 21:00 UT. (e) The square of the vertical wavenumber m^2 derived from the Brunt–Väisälä frequency N^2 and the average meteor radar wind profile in (d).

MGW was estimated to be approximately 1.08×10^{-5} W/m^2.

Accurately estimating the GW F_M and F_E is fundamental because these quantities directly quantify how waves transport momentum and energy from their source regions into the middle and upper atmosphere, driving large-scale circulation and influencing the thermal structure. Even if their magnitude is similar to waves from other sources, accurately estimating momentum and energy fluxes of jet-generated GWs holds paramount scientific importance. This is due to their distinct generation mechanism, geographic distribution, and climatic role. Unlike convectively generated GWs (thermal forcing, obstacle effect, and mechanical oscillator effect; Fritts and Alexander, 2003) or orographic GWs (fixed mechanical forcing), jets produce GWs through baroclinic instability and shear, making them a primary wave source along midlatitude storm tracks. Accurately quantifying their flux is therefore critical for understanding and modeling their specific, dominant contribution to driving the general circulation models in these regions, which remains a key source of uncertainty in general circulation models owing to inadequate GW parameterization.

In this context, the momentum and energy fluxes quantified in this study (~24.93 m^2/s^2 and ~1.08×10^{-5} W/m^2, respectively) provide a concrete observational benchmark for such intense jet-generated wave events. The relatively large momentum flux, compared with those from polar jets and jet–front systems, indicates an exceptionally strong source intensity associated with the subtropical jet adjacent to the Tibetan Plateau. This likely reflects a vigorous dynamical interaction between the jet stream and the unique topography or baroclinicity of the region, leading to efficient momentum extraction. Furthermore, the substantial energy flux signifies a significant potential for vertical energy transport. If these waves propagate to the MLT, they are capable of depositing considerable momentum and energy, thereby contributing to modulation of the circulation and thermal structure at those altitudes—a process that is critical yet poorly constrained in models. This case thus highlights both the role of the Tibetan Plateau region as a potent wave source and the value of direct flux quantification for improving our mechanistic understanding and model representation of these dynamics.

3.2 Source Localization of the MGW via Reverse Ray Tracing

We applied the backward ray-tracing technique described by Marks and Eckermann (1995) to study the source of the MGW. The equations are given by

$$C_{gx} = \frac{\mathrm{d}x}{\mathrm{d}t} = \frac{k_x(N^2 - \hat{\omega}^2)}{\hat{\omega}\Delta} + U, \tag{5}$$

$$C_{gy} = \frac{\mathrm{d}y}{\mathrm{d}t} = \frac{k_y(N^2 - \hat{\omega}^2)}{\hat{\omega}\Delta} + V, \tag{6}$$

$$C_{gz} = \frac{\mathrm{d}z}{\mathrm{d}t} = -\frac{m(\hat{\omega}^2 - f^2)}{\hat{\omega}\Delta}, \tag{7}$$

where C_{gx},C_{gy}, and C_{gz} represent the ground-based zonal, meridional, and vertical group velocities, respectively; $\Delta = k_x^2 + k_y^2 + m^2 + a^2$, where $a^2 = \frac{1}{4H^2}$ and k_x and k_y are the zonal and meridional wavenumbers, respectively; $\hat{\omega} = \omega_o - Uk_x - Vk_y$, where ω_o is the ground-based wave frequency; U and V are background wind velocities in the zonal and meridional wind, respectively; and f is the Coriolis parameter (inertial frequency). The background temperature and wind profiles are derived from ERA5 reanalysis data. For the purposes of this study, the time step is defined as 100 m/C_{gz}. The ray-tracing paths terminated under the following conditions: (1) when m^2 becomes negative, the wave becomes evanescent and cannot propagate vertically; (2) when m^2 becomes larger than 4.0×10^{-5} rad^2/m^2, it indicates that the wave is approaching a critical level; (3) when the intrinsic frequency approaches zero or becomes negative, it signifies that the wave is approaching (or has encountered) a critical level where the wave packet is likely to break, as described by Wrasse et al. (2006).

Figure 5 presents the input background data for backward ray tracing on January 12, 2010, with temperature sourced from the ERA5 reanalysis (0–80 km). In this study, the starting height of the backward ray tracing was 80 km.

Figure 6 shows the results of the backward ray-tracing paths. The MGW was traced back to the northeast corner of the Tibetan Plateau at (34.69 ± 0.5°N, 106.46 ± 1.2°E), approximately 1030–1274 km away from Xinglong. The wave took 3.7 ± 0.4 h to propagate from 81 km to 9.1 ± 3 km along the path.

According to the linear dispersion theory, high-frequency waves obey $\tan\phi = \lambda_z/\lambda_h$, where ϕ is the propagation angle of the wave relative to the horizontal direction. On the basis of this dispersion relation and the observed wavelength parameters, the estimated horizontal propagation distance is approximately 950 to 1115 km. This result is in close agreement with the horizontal propagation distance confirmed by the ray-tracing analysis. The close agreement between the horizontal propagation distance estimated from linear dispersion theory and that obtained from the ray-tracing analysis serves as a key internal validation of the physical plausibility of the model.

3.3 Generation Mechanisms of the MGW

Convective systems are considered widespread sources of GWs. To assess whether the observed MGW originated from convection, we analyzed the convective intensity by using ERA5 reanalysis data (Hersbach et al., 2020) from the ECMWF. The vertical velocity at 300 hPa (~9.2 km altitude), shown in Figure 7, serves as a proxy for convective activity strength. At the ray-traced MGW source location (cross marker, Figure 7), vertical velocity values indicate weak convection. Consequently, we conclude that convection did not generate the airglow-observed MGW.

The significance of topography as a source of GW generation must be emphasized, particularly in the case of the Tibetan Plateau, the highest plateau on Earth. When air flows over mountainous terrain, it excites mountain waves, which constitute a specific type of GWs (Inchin et al., 2024; Wei JR et al., 2024). These waves propagate against the background wind and appear quasi-stationary to a ground-based observer. However, our airglow imaging observations revealed freely propagating wave struc-

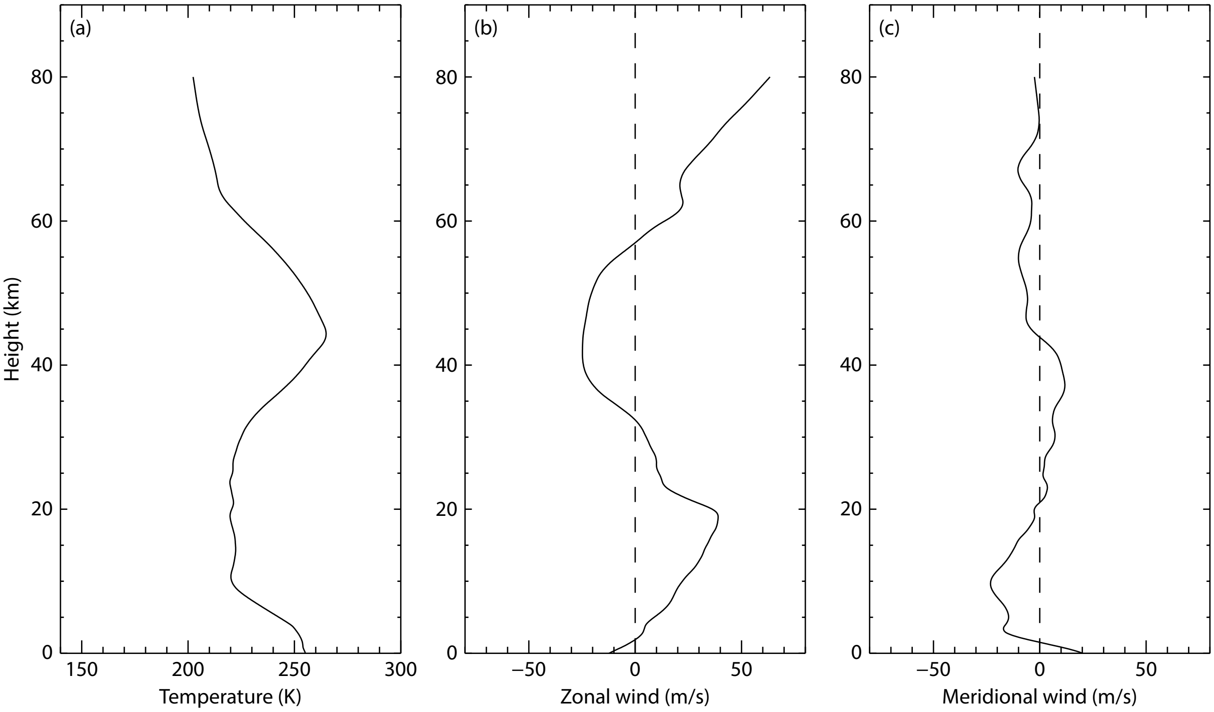

Figure 5. (a) Temperature, (b) zonal wind, and (c) meridional wind derived from the ERA5 reanalysis on January 12, 2010. The data represent a 4-h mean between 15:00 and 19:00 UT.

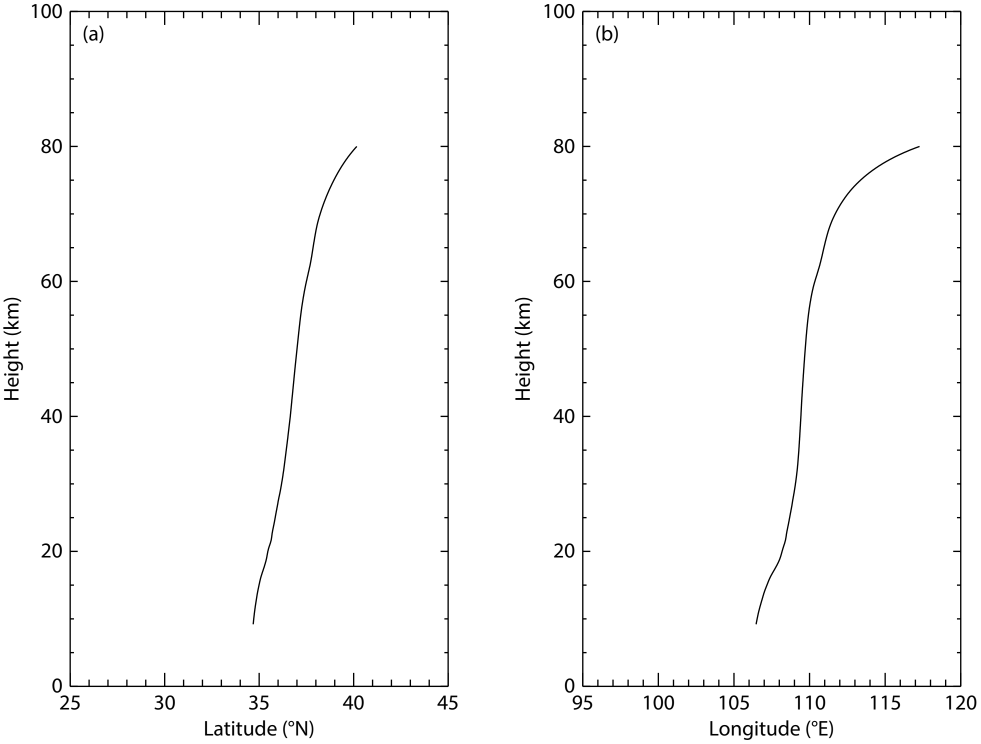

Figure 6. The backward ray-tracing calculation paths for (a) latitude–altitude and (b) longitude–altitude.

tures. Therefore, topography can be confidently excluded as the source of the MGW detected in this study.

Tropospheric jet systems are established sources of GWs in the mesosphere, as demonstrated by numerical simulations and observations (Fritts and Nastrom, 1992; Zhang FQ, 2004; Plougonven and Snyder, 2005).

Figure 8 displays the horizontal wind fields at 300 hPa (~9.2 km altitude) from the ERA5 reanalysis at 15:00 UT on January 12, 2010. A prominent tropospheric winter jet with core zonal winds exceeding 90 m/s traverses the Tibetan Plateau, with the ray-

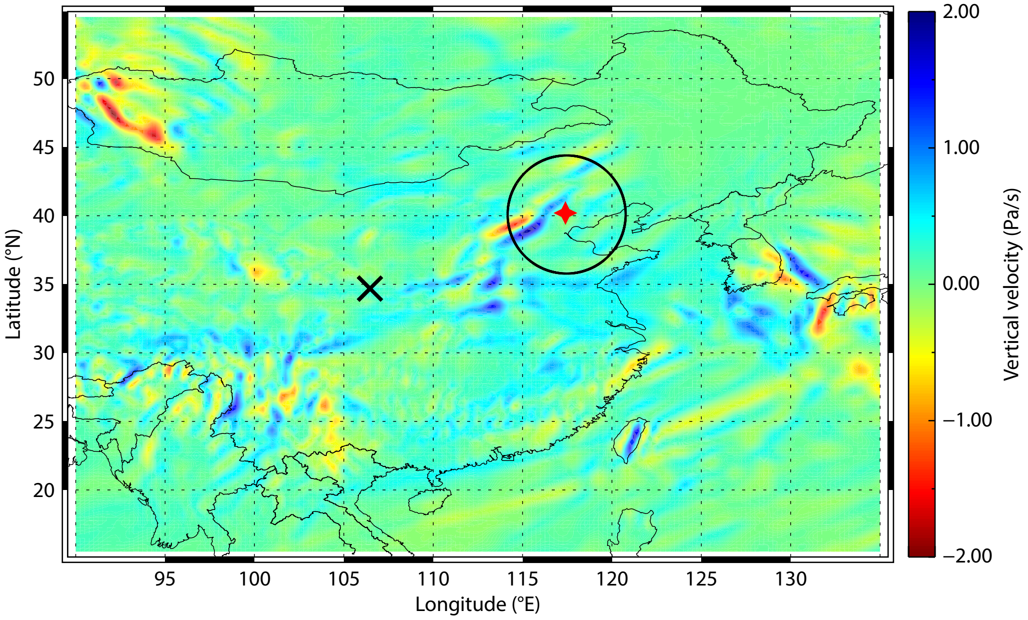

Figure 7. The tropospheric vertical flow velocity at 300 hPa (~9.2 km altitude) obtained by the ERA5 from the ECMWF. A negative pressure vertical velocity (upward motion) indicates relatively strong convective activity. The circle gives the effective observation ranges of the OH airglow imager, with a diameter of approximately 800 km. The cross marks the location of the wave source obtained from ray tracing.

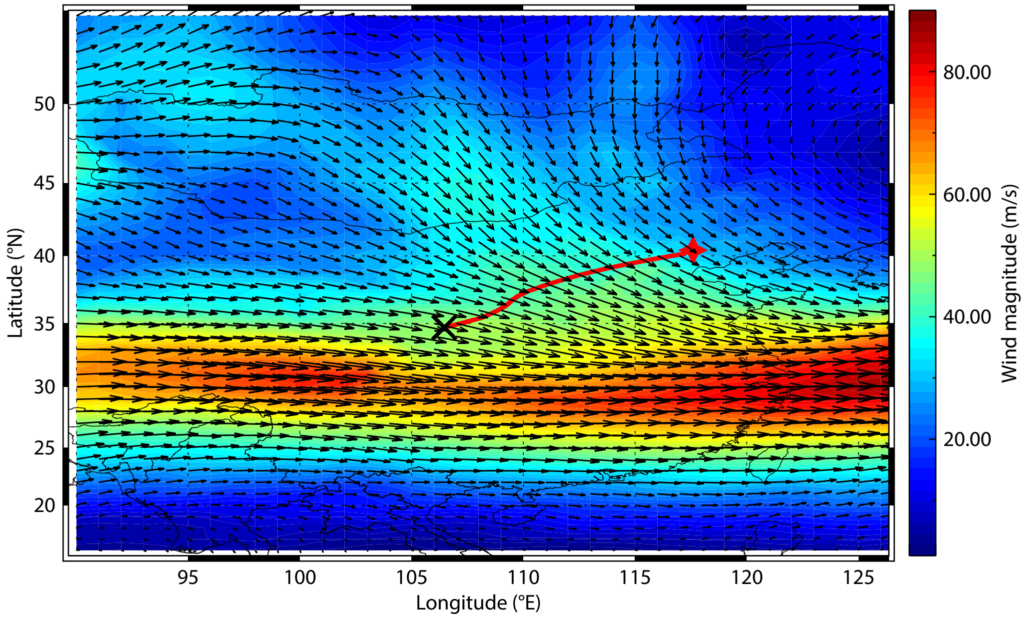

Figure 8. Map of the wind vectors at pressure levels of 300 hPa obtained by the ERA5 reanalysis model at 15:00 UT on January 12, 2010. The red star indicates the location of the Xinglong station. The cross marks the location of the wave source obtained from ray tracing.

traced source of the MGW located near its northeastern margin (cross marker). This positioning is consistent with numerous case studies that have reported intense GW activity occurring in the vicinity of jet–front systems (Plougonven and Zhang FQ, 2014). Nevertheless, the precise mechanisms of GW generation near jets and fronts remain debated, with proposed candidates encompassing geostrophic adjustment, Lighthill radiation, various instabilities, transient growth, and convections (Plougonven and Zhang FQ, 2014). Geostrophic adjustment processes can generate only low-frequency (on the order of a few tens of hours or more) planetary-scale waves but not high-frequency GWs like the ones (periodicity of a few tens of minutes) detected in the present OH images.

Given that the mere existence of jet stream winds alone is insufficient for GW generation—and that such waves are primarily excited by instabilities within the flow—we therefore investigated the characteristics of potential instabilities in the source region by using the Richardson number (*Ri*; Richardson, 1920). This parameter, defined as

$$Ri=\frac{N^2}{(\mathrm{d}U/\mathrm{d}z)^2+(\mathrm{d}V/\mathrm{d}z)^2},$$

represents the ratio of stabilizing buoyancy forces to destabilizing vertical wind shear. Dynamical instabilities, such as the Kelvin–Helmholtz instability (KHI), are favored in layers where $0 < Ri < 0.25$, whereas $Ri < 0$ indicates convective instability (Beer, 1974). Our calculations of the Richardson number Ri using ERA5 data confirmed that values in the ray termination region were greater than the critical threshold of 0.25. This result indicates that neither convective nor shear instability (KHI) was present, thereby ruling out these mechanisms as direct energy sources for the observed phenomena.

This finding, however, directs us to a more fundamental generation mechanism: spontaneous GW emission during rapid adjustment of the horizontally sheared jet flank. The core of the jet stream is in near-geostrophic balance, but its flanks are characterized by intense horizontal shear and strong vorticity gradients—a region of inherent flow susceptibility and a known source for GWs near jet–front systems (Plougonven and Zhang FQ, 2014). This zone hosts persistent potential vorticity anomalies, and any rapid modification—such as that from diabatic processes or interaction with transients—can disrupt this tight balance and trigger a swift, localized adjustment (O'Sullivan and Dunkerton, 1995). Unlike slow, large-scale geostrophic adjustment, this process—driven by horizontal shear instability and transient imbalance—readily radiates excess energy as inertia GWs, including high-frequency components with periods of tens of minutes. Our reverse ray-tracing result, which terminates precisely in this zone of maximum horizontal shear and vorticity, and not at the wind maximum, strongly indicates that this site was an active source of such a shear-driven adjustment process.

We also examined the vertical velocity and horizontal wind vectors at different altitudes to further identify the excitation source of the MGW. Figures 9a–9d present the distribution of vertical velocity in the altitude range of 6 to 12 km, revealing relatively weak convective activity near the ray-traced source of the MGW. Figures 9e–9h show the distribution of horizontal wind vectors between 6 and 12 km, indicating a strong jet near the ray-traced source of the MGW, particularly at the 225 hPa (~11.0 km) and 175 hPa (~12.6 km) levels.

3.4 Mechanisms of Ripple Formation

As shown above, ripples were generated during propagation of the GWs. We used meteor radar to investigate the characteristics of the background wind field. The hodograph in Figure 10a reveals that the wind direction was almost aligned with the wave propagation direction. The vector plot in Figure 10b shows that during the period of 19:00–21:00 UT, there was strong wind shear from an altitude of 80 to 88 km, with the wind speed increasing from an average of 13 m/s at 80 km to 86 m/s at 88 km. This strong shear likely induced dynamical instability in the MLT region, resulting in the observed ripples. Theoretical and observational studies (Fritts et al., 1997; Hecht et al., 1997; Li T et al., 2005; Li J et al., 2017) have revealed that convectively generated ripples exhibit phase fronts perpendicular to their parent GW, whereas ripples arising from dynamical instabilities maintain phase fronts parallel to the breaking GW.

Hecht (2004) proposed that wind shear can detach instability-generated ripples from their parent GWs and rotate them, potentially reorienting the ripples to be perpendicular to the GW fronts; this mechanism explains the observed misalignment and likely reduces the occurrence of parallel alignments.

4. Summary

In this work, we report on an MGW observed by the OH airglow imager at the Xinglong station in northern China on the night of January 12, 2010. The MGW propagated from west to east, with a horizontal wavelength of 125 ± 7.6 km, an observed period of 25 ± 3.2 min, and a phase speed of 83 ± 12.4 m/s. We estimated that the momentum flux and the energy flux of the GW were approximately 24.93 $\mathrm{m^2/s^2}$ and 1.08×10^{-5} $\mathrm{W/m^2}$, respectively. We also observed a small-scale GW propagating northwestward, exhibiting a horizontal wavelength of approximately 35 km, a period of 16 min, and a phase speed of 36 m/s. To investigate the MGW source, a backward ray-tracing analysis was performed by combining data with satellite temperature profiles from the TIMED/SABER satellite. The results, supported by ERA5 reanalysis data, indicate that the MGW was likely generated by a jet system near the Tibetan Plateau. Concurrently with the primary MGW, we observed small-scale structures (5–12 km wavelength ripples) identified as wind shear-induced dynamic instabilities. The observed angular divergence aligns with predictions of instabilities being reoriented toward perpendicularity with parent waves through shear-mediated processes, thereby reducing parallel alignment scenarios.

Our observations captured a remarkable spectrum of atmospheric waves over northern China, spanning spatial scales from ~5 to ~125 km, alongside direct evidence of wave breaking. This multiscale activity, particularly the observed wave breaking, strongly implies significant vertical energy and momentum transport within the local atmosphere. Such processes are crucial for understanding and accurately parameterizing the forcing of the mean flow, turbulence generation, and resultant mixing that regulates the atmospheric structure and stability in the MLT region.

Acknowledgements

This work was supported by the B-type Strategic Priority Program of the Chinese Academy of Sciences (CAS; Grant No. XDB0780000), as well as the National Natural Science Foundation of China (Grant Nos. 42374205 and 41974179) and the Specialized Research Fund of the National Space Science Center, CAS (Grant No. E4PD3010). The project was also supported by the Specialized Research Fund for State Key Laboratories. We acknowledge the use of data from the Chinese Meridian Project.

References

Alexander, M. J., and Holton, J. R. (2004). On the spectrum of vertically propagating gravity waves generated by a transient heat source. *Atmos. Chem. Phys.*, *4*(4), 923–932. https://doi.org/10.5194/acp-4-923-2004

Beer, T. (1974). *Atmospheric Waves*. New York: Wiley.

Chen, Y. X., Lai, C., Li, Q. Z., Xu, J. Y., and Yuan, W. (2026). Comparison of

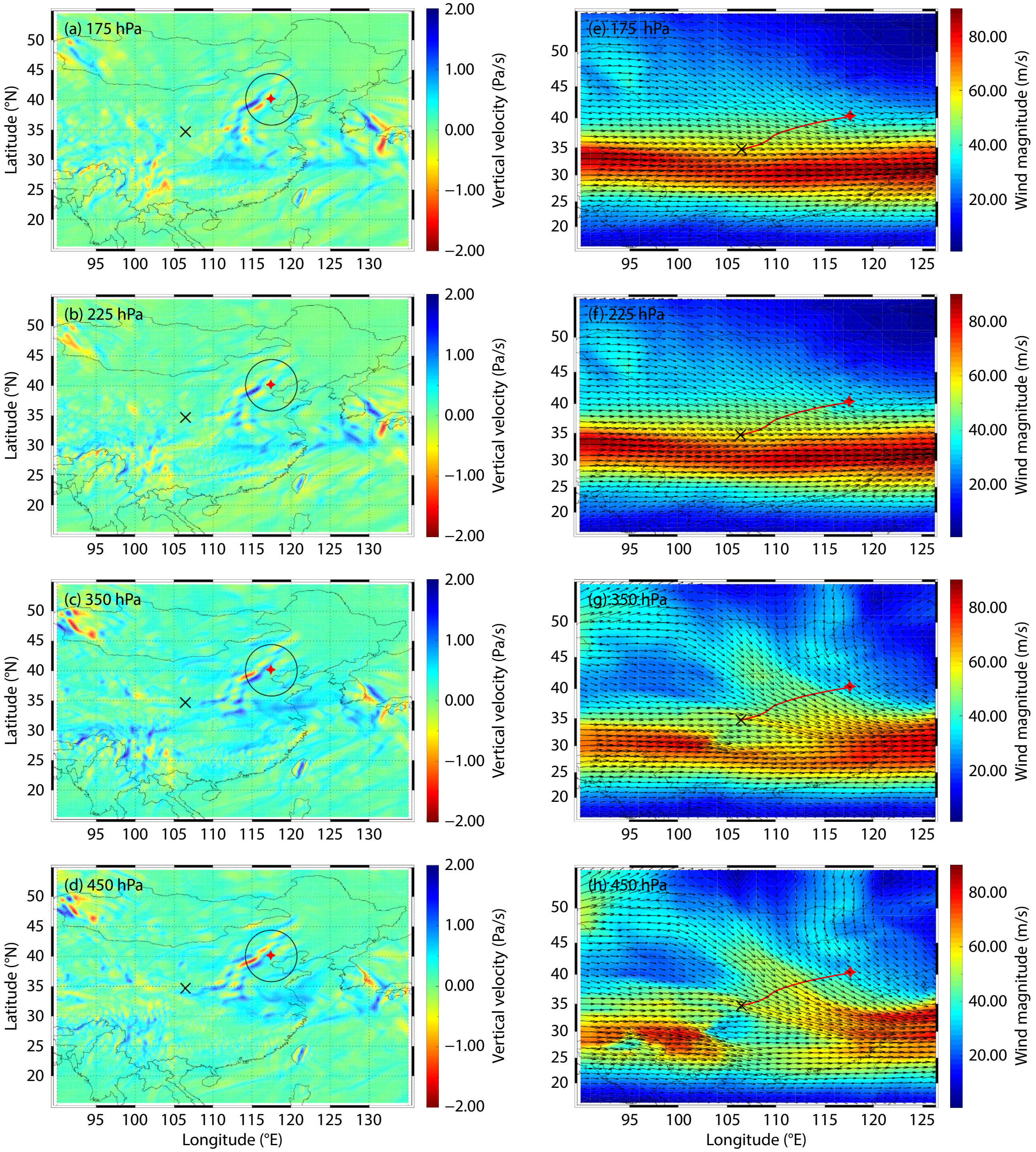

Figure 9. (a–d) Vertical velocity and (e–h) horizontal wind vectors at 175 hPa (~12.6 km), 225 hPa (~11.0 km), 350 hPa (~8.1 km), and 450 hPa (~6.3 km) from the ERA5 reanalysis at 15:00 UT on January 12, 2010.

atmospheric gravity wave event statistics between Dandong and Lhasa. *Earth Planet. Phys.*, *10*(1), 176–185. https://doi.org/10.26464/epp2026002

Chen, G., Zhao, Z. Y., Zhang, Y. N., Yang, G. B., Zhou, C., Huang, S., Li, T., Li, N., and Sun, H. Q. (2011). Gravity waves and spread *Es* observed during the solar eclipse of 22 July 2009. *J. Geophys. Res.: Space Phys.*, *116*(A9), A09314. https://doi.org/10.1029/2011JA016720

Ejiri, M. K., Shiokawa, K., Ogawa, T., Igarashi, K., Nakamura, T., and Tsuda, T. (2003). Statistical study of short-period gravity waves in OH and OI nightglow images at two separated sites. *J. Geophys. Res.: Atmos.*, *108*(D21), 4679. https://doi.org/10.1029/2002JD002795

Ern, M., Preusse, P., and Riese, M. (2022). Intermittency of gravity wave potential energies and absolute momentum fluxes derived from infrared limb sounding satellite observations. *Atmos. Chem. Phys.*, *22*(22), 15093–15133. https://doi.org/10.5194/acp-22-15093-2022

Fovell, R., Durran, D., and Holton, J. R. (1992). Numerical simulations of convectively generated stratospheric gravity waves. *J. Atmos. Sci.*, *49*(16), 1427–1442. https://doi.org/10.1175/1520-0469(1992)049<1427:NSOCGS>2.0.CO;2

Franco-Diaz, E., Gerding, M., Holt, L., Strelnikova, I., Wing, R., Baumgarten, G., and Lübken, F. J. (2024). Convective gravity wave events during summer

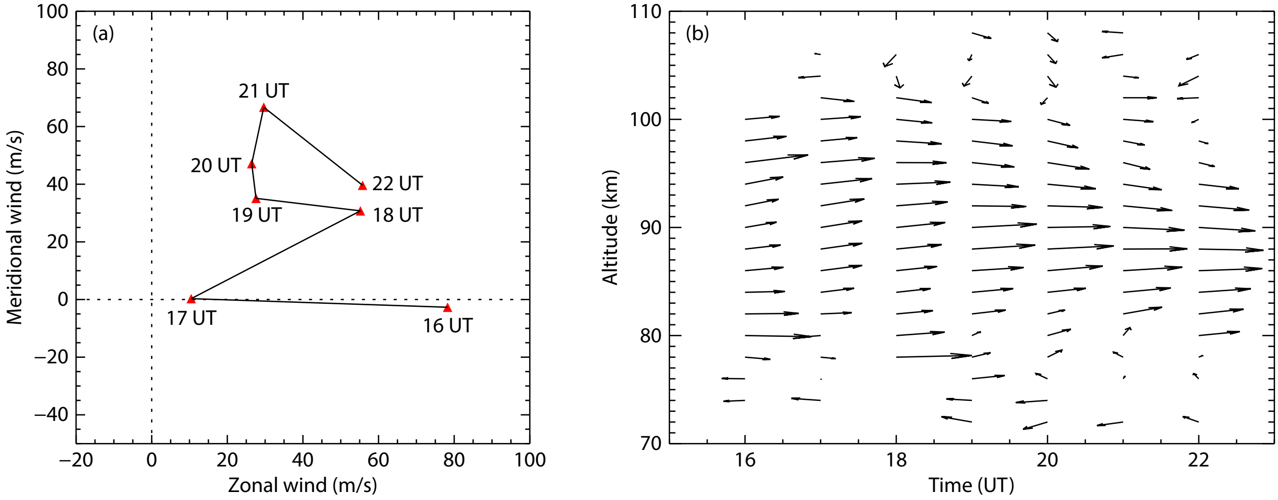

Figure 10. Mesospheric wind characteristics derived from meteor radar at the Shisanling station on January 12, 2010. (a) Hodograph of the wind at an altitude of 81 km. (b) Vector plot of the horizontal wind component (up is northward, right is eastward).

near 54° N, present in both AIRS and Rayleigh–Mie–Raman (RMR) lidar observations. *Atmos. Chem. Phys., 24*(2), 1543–1558. https://doi.org/10.5194/acp-24-1543-2024

Fritts, D. C. (1982). Shear excitation of atmospheric gravity waves. *J. Atmos. Sci.*, *39*(9), 1936–1952. https://doi.org/10.1175/1520-0469(1982)039<1936:SEOAGW>2.0.CO;2

Fritts, D. C., and Nastrom, G. D. (1992). Sources of mesoscale variability of gravity waves. Part II: Frontal, convective, and jet stream excitation. *J. Atmos. Sci., 49*(2), 111–127. https://doi.org/10.1175/1520-0469(1992)049<0111:SOMVOG>2.0.CO;2

Fritts, D. C., Isler, J. R., Hecht, J. H., Walterscheid, R. L., and Andreassen, Ø. (1997). Wave breaking signatures in sodium densities and OH nightglow: 2. Simulation of wave and instability structures. *J. Geophys. Res.: Atmos.*, *102*(D6), 6669–6684. https://doi.org/10.1029/96JD01902

Fritts, D. C., and Alexander, M. J. (2003). Gravity wave dynamics and effects in the middle atmosphere. *Rev. Geophys.*, *41*(1), 1003. https://doi.org/10.1029/2001RG000106

Gao, H. Y., Li, L. C., Bu, L. B., Zhang, Q. L., Tang, Y. H., and Wang, Z. (2018). Effect of small-scale gravity waves on polar mesospheric clouds observed from CIPS/AIM. *J. Geophys. Res.: Space Phys.*, *123*(5), 4026–4045. https://doi.org/10.1029/2017JA024855

Garcia, F. J., Taylor, M. J., and Kelley, M. C. (1997). Two-dimensional spectral analysis of mesospheric airglow image data. *Appl. Opt.*, *36*(29), 7374–7385. https://doi.org/10.1364/AO.36.007374

Gavrilov, N. M., Kshevetskii, S. P., and Koval, A. V. (2022). Decay times of atmospheric acoustic–gravity waves after deactivation of wave forcing. *Atmos. Chem. Phys.*, *22*(20), 13713–13724. https://doi.org/10.5194/acp-22-13713-2022

Geldenhuys, M., Preusse, P., Krisch, I., Zülicke, C., Ungermann, J., Ern, M., Friedl-Vallon, F., and Riese, M. (2021). Orographically induced spontaneous imbalance within the jet causing a large-scale gravity wave event. *Atmos. Chem. Phys.*, *21*(13), 10393–10412. https://doi.org/10.5194/acp-21-10393-2021

Ghodpage, R. N., Hickey, M. P., Taori, A. K., Siingh, D., and Patil, P. T. (2016). Response of OH airglow emissions to mesospheric gravity waves and comparisons with full-wave model simulation at a low-latitude Indian station. *Atmos. Chem. Phys.*, *16*(9), 5611–5621. https://doi.org/10.5194/acp-16-5611-2016

Gu, S. Y., Yang, Z. L., Qin, Y. S., Teng, C. K. M., Dou, X. K., Lei, J. H., Huang, F. Q., Dang, T., and Sun, W. J. (2023). Ionospheric TEC variation and gravity waves signatures during the solar eclipse on 21 June 2020 over southern China. *J. Geophys. Res.: Space Phys.*, *128*(1), e2022JA030758. https://doi.org/10.1029/2022JA030758

Hapgood, M. A., and Taylor, M. J. (1982). Analysis of airglow image data. *Ann. Geophys.*, *38*, 805–813.

Hecht, J. H., Walterscheid, R. L., Fritts, D. C., Isler, J. R., Senft, D. C., Gardner, C. S., and Franke, S. J. (1997). Wave breaking signatures in OH airglow and sodium densities and temperatures: 1. Airglow imaging, Na lidar, and MF radar observations. *J. Geophys. Res.: Atmos.*, *102*(D6), 6655–6668. https://doi.org/10.1029/96JD02619

Hecht, J. H. (2004). Instability layers and airglow imaging. *Rev. Geophys.*, *42*(1), RG1001. https://doi.org/10.1029/2003RG000131

Hersbach, H., Bell, B., Berrisford, P., Hirahara, S., Horányi, A., Muñoz-Sabater, J., Nicolas, J., Peubey, C., Radu, R., … Thépaut, J. N. (2020). The ERA5 global reanalysis. *Quart. J. Roy. Meteor. Soc.*, *146*(730), 1999–2049. https://doi.org/10.1002/qj.3803

Hines, C. O. (1960). Internal atmospheric gravity waves at ionospheric heights. *Can. J. Phys.*, *38*(11), 1441–1481. https://doi.org/10.1139/p60-150

Holdsworth, D. A., Reid, I. M., and Cervera, M. A. (2004). Buckland Park all-sky interferometric meteor radar. *Radio Sci.*, *39*(5), RS5009. https://doi.org/10.1029/2003RS003014

Inchin, P. A., Bhatt, A., Bramberger, M., Chakraborty, S., Debchoudhury, S., and Heale, C. (2024). Atmospheric and ionospheric responses to orographic gravity waves prior to the December 2022 cold air outbreak. *J. Geophys. Res.: Space Phys.*, *129*(6), e2024JA032485. https://doi.org/10.1029/2024JA032485

Jia, M. J., Xue, X. H., Dou, X. K., Tang, Y. H., Yu, C., Wu, J. F., Xu, J. Y., Yang, G. T., Ning, B. Q., and Hoffmann, L. (2016). A case study of a mesoscale gravity wave in the MLT region using simultaneous multi-instruments in Beijing. *J. Atmos. Sol.-Terr. Phys.*, *140*, 1–9. https://doi.org/10.1016/j.jastp.2016.01.007

Kubota, M., Fukunishi, H., and Okano, S. (2001). Characteristics of medium- and large-scale TIDs over Japan derived from OI 630-nm nightglow observation. *Earth Planets Space*, *53*(7), 741–751. https://doi.org/10.1186/BF03352402

Li, J., Li, T., Dou, X. K., Fang, X., Cao, B., She, C. Y., Nakamura, T., Manson, A., Meek, C., and Thorsen, D. (2017). Characteristics of ripple structures revealed in OH airglow images. *J. Geophys. Res.: Space Phys.*, *122*(3), 3748–3759. https://doi.org/10.1002/2016JA023538

Li, Q. Z., Xu, J. Y., Yue, J., Yuan, W., and Liu, X. (2011). Statistical characteristics of gravity wave activities observed by an OH airglow imager at Xinglong, in northern China. *Ann. Geophys.*, *29*(8), 1401–1410. https://doi.org/10.5194/angeo-29-1401-2011

Li, Q. Z., Xu, J. Y., Liu, X., Yuan, W., and Chen, J. S. (2016). Characteristics of mesospheric gravity waves over the southeastern Tibetan Plateau region. *J. Geophys. Res.: Space Phys.*, *121*(9), 9204–9221. https://doi.org/10.1002/2016JA022823

Li, Q. Z., Yusupov, K., Akchurin, A., Yuan, W., Liu, X., and Xu, J. Y. (2018). First OH airglow observation of mesospheric gravity waves over European Russia region. *J. Geophys. Res.: Space Phys.*, *123*(3), 2168–2180. https://doi.org/10.1002/2017JA025081

Li, Q. Z., Xu, J. Y., Liu, H. L., Liu, X., and Yuan, W. (2022). How do gravity waves triggered by a typhoon propagate from the troposphere to the upper atmosphere?. *Atmos. Chem. Phys.*, *22*(18), 12077–12091. https://doi.org/10.5194/acp-22-12077-2022

Li, Q. Z., Xu, J. Y., Gusman, A. R., Liu, H. L., Yuan, W., Liu, W. J., Zhu, Y. J., and Liu, X. (2024). Upper-atmosphere responses to the 2022 Hunga Tonga–Hunga Ha'apai volcanic eruption via acoustic gravity waves and air–sea interaction. *Atmos. Chem. Phys.*, *24*(14), 8343–8361. https://doi.org/10.5194/acp-24-8343-2024

Li, Q. Z., Xu, J. Y., Zhu, Y. J., Wrasse, C. M., Bageston, J. V., Yuan, W., Liu, X., Liu, W. J, Wen, Y., … Liu, Z. K. (2025a). Extreme concentric gravity waves observed in the mesosphere and thermosphere regions over southern Brazil associated with fast-moving severe thunderstorms. *Atmos. Chem. Phys.*, *25*(17), 9719–9736. https://doi.org/10.5194/acp-25-9719-2025

Li, Q. Z., Xu, J. Y., Yuan, W., Liu, X., Zhu, Y. J., and Liu, W. J. (2025b). Three-dimensional spectral analysis of gravity waves from airglow observations over Northwest China. *Earth Planet. Phys.*, *9*(4), 988–994. https://doi.org/10.26464/epp2025050

Li, T., She, C. Y., Williams, B. P., Yuan, T., Collins, R. L., Kieffaber, L. M., and Peterson, A. W. (2005). Concurrent OH imager and sodium temperature/wind lidar observation of localized ripples over northern Colorado. *J. Geophys. Res.: Atmos.*, *110*(D13), D13110. https://doi.org/10.1029/2004JD004885

Marks, C. J., and Eckermann, S. D. (1995). A three-dimensional nonhydrostatic ray-tracing model for gravity waves: Formulation and preliminary results for the middle atmosphere. *J. Atmos. Sci.*, *52*(11), 1959–1984. https://doi.org/10.1175/1520-0469(1995)052<1959:ATDNRT>2.0.CO;2

Mertens, C. J., Mlynczak, M. G., López-Puertas, M., Wintersteiner, P. P., Picard, R. H., Winick, J. R., Gordley, L. L., and Russell, J. M. (2001). Retrieval of mesospheric and lower thermospheric kinetic temperature from measurements of CO_2 15 μm Earth Limb Emission under non-LTE conditions. *Geophys. Res. Lett.*, *28*(7), 1391–1394. https://doi.org/10.1029/2000GL012189

Nayak, C., and Yiğit, E. (2018). GPS-TEC observation of gravity waves generated in the ionosphere during 21 August 2017 total solar eclipse. *J. Geophys. Res.: Space Phys.*, *123*(1), 725–738. https://doi.org/10.1002/2017JA024845

Nielsen, K., Taylor, M. J., Hibbins, R. E., and Jarvis, M. J. (2009). Climatology of short-period mesospheric gravity waves over Halley, Antarctica (76°S, 27°W). *J. Atmos. Sol.-Terr. Phys.*, *71*(8-9), 991–1000. https://doi.org/10.1016/j.jastp.2009.04.005

Nyassor, P. K., Wrasse, C. M., Paulino, I., São Sabbas, E. F. M. T., Bageston, J. V., Naccarato, K. P., Gobbi, D., Figueiredo, C. A. O. B., Ayorinde, T. T., … Barros, D. (2022). Sources of concentric gravity waves generated by a moving mesoscale convective system in southern Brazil. *Atmos. Chem. Phys.*, *22*(23), 15153–15177. https://doi.org/10.5194/acp-22-15153-2022

Nyassor, P. K., Wrasse, C. M., Paulino, I., Yiğit, E., Tsali-Brown, V. Y., Buriti, R. A., Figueiredo, C. A. O. B., Giongo, G. A., Egito, F., … Gobbi, D. (2025). Momentum flux characteristics of vertically propagating gravity waves. *Atmos. Chem. Phys.*, *25*(7), 4053–4082. https://doi.org/10.5194/acp-25-4053-2025

O'Sullivan, D., and Dunkerton, T. J. (1995). Generation of inertia-gravity waves in a simulated life cycle of baroclinic instability. *J. Atmos. Sci.*, *52*(21), 3695–3716. https://doi.org/10.1175/1520-0469(1995)052<3695:GOIWIA>2.0.CO;2

Plane, J. M. C., Gumbel, J., Kalogerakis, K. S., Marsh, D. R., and von Savigny, C. (2023). Opinion: Recent developments and future directions in studying the mesosphere and lower thermosphere. *Atmos. Chem. Phys.*, *23*(20), 13255–13282. https://doi.org/10.5194/acp-23-13255-2023

Plougonven, R., and Snyder, C. (2005). Gravity waves excited by jets: Propagation versus generation. *Geophys. Res. Lett.*, *32*(18), L18802. https://doi.org/10.1029/2005GL023730

Plougonven, R., and Zhang, F. Q. (2014). Internal gravity waves from atmospheric jets and fronts. *Rev. Geophys.*, *52*(1), 33–76. https://doi.org/10.1002/2012RG000419

Pramitha, M., Venkat Ratnam, M., Taori, A., Krishna Murthy, B. V., Pallamraju, D., and Vijaya Bhaskar Rao, S. (2015). Evidence for tropospheric wind shear excitation of high-phase-speed gravity waves reaching the mesosphere using the ray-tracing technique. *Atmos. Chem. Phys.*, *15*(5), 2709–2721. https://doi.org/10.5194/acp-15-2709-2015

Richardson, L. F. (1920). The supply of energy from and to atmospheric eddies. *Proc. Roy. Soc. A*, *97*(686), 354–373. https://doi.org/10.1098/rspa.1920.0039

Smith, S. M., Mendillo, M., Baumgardner, J., and Clark, R. R. (2000). Mesospheric gravity wave imaging at a subauroral site: First results from Millstone Hill. *J. Geophys. Res.: Space Phys.*, *105*(A12), 27119–27130. https://doi.org/10.1029/1999JA000343

Suzuki, S., Shiokawa, K., Otsuka, Y., Ogawa, T., Kubota, M., Tsutsumi, M., Nakamura, T., and Fritts, D. C. (2007). Gravity wave momentum flux in the upper mesosphere derived from OH airglow imaging measurements. *Earth Planets Space*, *59*(5), 421–428. https://doi.org/10.1186/BF03352703

Suzuki, S., Lübken, F. J., Baumgarten, G., Kaifler, N., Eixmann, R., Williams, B. P., and Nakamura, T. (2013). Vertical propagation of a mesoscale gravity wave from the lower to the upper atmosphere. *J. Atmos. Sol.-Terr. Phys.*, *97*, 29–36. https://doi.org/10.1016/j.jastp.2013.01.012

Swenson, G. R., and Liu, A. Z. (1998). A model for calculating acoustic gravity wave energy and momentum flux in the mesosphere from OH airglow. *Geophys. Res. Lett.*, *25*(4), 477–480. https://doi.org/10.1029/98GL00132

Wei, J. R., Liu, X., Xu, J. Y., Li, Q. Z., and Gao, H. (2024). Influence of topography on the fine structures of stratospheric gravity waves: An analysis using COSMIC-2 temperature data. *Earth Planet. Phys.*, *8*(3), 497–513. https://doi.org/10.26464/epp2024027

Wrasse, C. M., Nakamura, T., Tsuda, T., Takahashi, H., Medeiros, A. F., Taylor, M. J., Gobbi, D., Salatun, A., Suratno, … Admiranto, A. G. (2006). Reverse ray tracing of the mesospheric gravity waves observed at 23°S (Brazil) and 7°S (Indonesia) in airglow imagers. *J. Atmos. Sol.-Terr. Phys.*, *68*(2), 163–181. https://doi.org/10.1016/j.jastp.2005.10.012

Wrasse, C. M., Nyassor, P. K., da Silva, L. A., Figueiredo, C. A. O. B., Bageston, J. V., Naccarato, K. P., Barros, D., Takahashi, H., and Gobbi, D. (2024). Studies on the propagation dynamics and source mechanism of quasi-monochromatic gravity waves observed over São Martinho da Serra (29° S, 53° W), Brazil. *Atmos. Chem. Phys.*, *24*(9), 5405–5431. https://doi.org/10.5194/acp-24-5405-2024

Wright, C. J., Hindley, N. P., Hoffmann, L., Alexander, M. J., and Mitchell, N. J. (2017). Exploring gravity wave characteristics in 3-D using a novel S-transform technique: AIRS/Aqua measurements over the Southern Andes and Drake Passage. *Atmos. Chem. Phys.*, *17*(13), 8553–8575. https://doi.org/10.5194/acp-17-8553-2017

Wüst, S., Schmidt, C., Hannawald, P., Bittner, M., Mlynczak, M. G., and Russell III, J. M. (2019). Observations of OH airglow from ground, aircraft, and satellite: Investigation of wave-like structures before a minor stratospheric warming. *Atmos. Chem. Phys.*, *19*(9), 6401–6418. https://doi.org/10.5194/acp-19-6401-2019

Wüst, S., Bittner, M., Espy, P. J., French, W. J. R., and Mulligan, F. J. (2023). Hydroxyl airglow observations for investigating atmospheric dynamics: Results and challenges. *Atmos. Chem. Phys.*, *23*(2), 1599–1618. https://doi.org/10.5194/acp-23-1599-2023

Xue, X. H., Sun, D. S., Xia, H. Y., and Dou, X. K. (2020). Inertial gravity waves observed by a Doppler wind LiDAR and their possible sources. *Earth Planet. Phys.*, *4*(5), 461–471 https://doi.org/10.26464/epp2020039

Zhang, F. Q. (2004). Generation of mesoscale gravity waves in upper-tropospheric jet–front systems. *J. Atmos. Sci.*, *61*(4), 440–457. https://doi.org/10.1175/1520-0469(2004)061<0440:GOMGWI>2.0.CO;2